ndt

MDPI

Article

Integrating 3D Polarimetric Ground Penetrating Radar and Augmented Reality for Reinforced Autoclaved Aerated Concrete Inspection

Samuel J. I. Forster [1,*], Daniel Conniffe [1], Anthony J. Peyton [1], Frank J. W. Podd [1] and Nigel Davidson [2] and Joshua B. Elliott [3]

[1] Department of Electrical and Electronic Engineering, The University of Manchester, Oxford Rd., Manchester M13 9PL, UK; daniel.conniffe@manchester.ac.uk (D.C.); a.peyton@manchester.ac.uk (A.J.P.); frank.podd@manchester.ac.uk (F.J.W.P.)
[2] Defence Science and Technology Laboratory, Porton Down, Salisbury SP4 0JQ, UK; ndavidson@mail.dstl.gov.uk
[3] The Manufacturing Technology Centre, Ansty Park, Coventry, West Midlands CV7 9JU, UK; joshua.elliott@the-mtc.org
* Correspondence: samuel.forster@postgrad.manchester.ac.uk

Abstract: Radar polarimetric imaging for non-destructive testing is a powerful and flexible tool that can be used to enhance the detection of internal structures. In this study, reinforced autoclaved aerated concrete (RAAC) is measured using a polarimetric system in three different acquisition modes—two downward-looking and one sideways-looking configurations, each at a different height. Each acquisition mode is compared and new polarisation states are created using the principle of polarisation synthesis. Images of the internal structures are created using a 3D imaging algorithm, which are used for the analysis. The comparison between acquisition modes demonstrates that using a higher lift-off and polarisation synthesis could offer more flexible operation in the field, allowing the use of handheld detectors and drone-based systems for inaccessible areas. Additionally, the sideways-looking data captured both horizontal and vertical reinforcement and were detected within a single polarisation channel; this configuration also has reduced clutter from the air–concrete boundary, providing a viable option for single polarisation systems.

Keywords: polarimetry; ground penetrating radar; synthetic aperture radar; augmented reality

Academic Editor: Fabio Tosti

Received: 22 November 2024
Revised: 9 January 2025
Accepted: 25 January 2025
Published: 28 January 2025

Citation: Forster, S.J.I.; Conniffe, D.; Peyton, A.J.; Podd, F.J.W.; Davidson, N.; Elliott, J.B. Integrating 3D Polarimetric Ground Penetrating Radar and Augmented Reality for Reinforced Autoclaved Aerated Concrete Inspection. *NDT* **2025**, *3*, 4. https://doi.org/10.3390/ndt3010004

1. Introduction

Reinforced autoclaved aerated concrete (RAAC) is a unique construction material that has been used in Europe since the 1950s and received global academic interest since the 1980s [1–3]. It is characterised by its aerated structure and absence of coarse aggregates, resulting in significantly different structural properties compared to traditional reinforced concrete. RAAC is approximately three to four times lighter than conventional concrete; this characteristic contributes to its lower compressive strength [4,5]. The aerated structure hinders solid reinforcement anchorage and increases permeability, making the material susceptible to water ingress and environmental effects. These factors, combined with the material's poor elasticity and creep resistance over time, pose challenges in its structural integrity [4,5]. Due to the inherent lack of structural robustness in autoclaved aerated concrete (AAC), the integrity of the embedded reinforcement is crucial to the strength of

RAAC. Understanding the condition of the reinforcement, such as its thickness, arrangement, and evidence of corrosion, is essential. This highlights the importance of the research presented in this paper, which supports efforts to address this critical industry need. In response to these issues, European standards were established in the 1990s in an attempt to ensure the long-term durability of RAAC structures [4,6–8]. Most of the current research has investigated inspection techniques for traditional reinforced concrete when compared to aerated concrete. Consequently, this paper incorporates inspection studies from both, as the inspection techniques would be transferable. The non-destructive assessment of RAAC panels is critical in evaluating structural safety and its condition whilst in situ. Non-destructive testing (NDT) techniques for reinforced concrete can be categorised into the following domains: ultrasonic, electrochemical, magnetic, and electromagnetic.

Ultrasonics have widely been used in assessing the structure of concrete, particularly for corrosion damage assessment and identifying cracks, although the heterogeneity of the concrete and issues with sensor coupling due to surface roughness can impact the accuracy of this method [9–12].

Electrochemical methods include the half-cell potential [13–15], electrochemical impedance spectroscopy [16–18], polarisation resistance measurements [19–21], and the galvanostatic pulse method [22–24]; these techniques are somewhat invasive and usually require holes to be drilled to directly connect probes to the reinforcement bars themselves.

Magnetic techniques such as magnetic flux leakage [25–27] and eddy current testing [28–30] are commonly used to assess the corrosion of the reinforcement bars; these methods are capable of detecting variations in the depth and diameter of the rebars [31]. However, they are generally less effective in assessing cracks and defects within the concrete itself, as these techniques primarily target the conductive and magnetic properties of the steel reinforcements.

Electromagnetic techniques, especially short-range, ultra-wideband radar, are widely used for various applications in concrete inspection, such as locating reinforcements, measuring the concrete cover thickness, and detecting corrosion. Ground penetrating radar (GPR) is one of the most commonly used technologies in this field and is often used as a general term for these radar-based techniques. Corroded reinforcement often manifests as a reduction in reflected energy and an increase in propagation delay [32–34]. Additionally, GPR can measure the radius of the reinforcement [35] and produce high-resolution images of the structure [36]. An investigation was conducted using angled GPR inspection with a dielectric wedge, focusing on the end-bearing regions of RAAC panels, a critical area in assessing RAAC's structural integrity [37]. While there are relatively few studies involving polarimetry, one such study found that corrosion shifted the scattering characteristics of the reinforcement from low-entropy dipole scattering to low-entropy surface scattering [38]. Other studies have used dual-polarisations but lack cross-polar receivers [39,40]. There is limited research using full polarimetric measurements for reinforced concrete inspection and none that the authors could find specifically using polarisation synthesis. This study aims to advance state-of-the-art techniques for the inspection of RAAC, using ceiling panels from educational estates, which can be classified as "in-service" artifacts, obtained from the Manufacturing Technology Centre (MTC). This contribution includes an investigation comparing surface and air-coupled antenna configurations along with downward- and sideways-looking geometries. A novel application of fully polarimetric GPR and polarisation synthesis is used to improve the detection of the reinforcement. It is shown that polarisation synthesis can be used to create an adaptable system that can reduce the orientation dependence of reinforcement and selectively filter for different features. The additional comparison between low/high liftoff and downward-/sideways-looking configurations illustrates the potential of these acquisition modes, highlighting the use of

GPR scanners without contact with the concrete, providing an equivalent resolution and performance. The non-contact modality is important due to the relatively common occurrence of asbestos-containing coatings that can be present on RAAC panels. Thus, avoiding disturbing these coatings has a significant health and safety benefit [41]. This research paves the way for the development of more flexible systems, potentially fusing polarisation synthesis and higher-lift-off geometries. Traditional scanning techniques have often used dual co-polar GPR systems in order to measure both horizontal and vertical sections of the reinforcement. The high-lift-off results, coupled with polarisation synthesis to remove the orientation angle dependence of these systems, will allow the use of handheld GPR scanners, as the operator will no longer be required to maintain the alignment with the horizontal and vertical reinforcement axes. Additionally, the high-lift-off results suggest, for certain scenarios, that drone-based systems could be used for the inspection of RAAC panels in less accessible locations.

2. Methodology

2.1. Experimental Setup

A stepped-frequency continuous-wave (SFCW) radar system was used for the data collection. This included a Copper Mountain Technologies (CMT) S5065 2-port vector network analyser (VNA) and a quad-ridged antenna (Astro Antenna AHA-118D). The antenna was dual-polarised and hence had two inputs, which were connected to the two ports of the VNA; the S-parameter measurements S11, S12, S22 correspond to the transmitted–received polarisations as horizontal–horizontal (HH), horizontal–vertical (HV), and vertical–vertical (VV), respectively. The VH polarisation is omitted since HV=VH due to the reciprocity of the mono-static configuration. The VNA was set up with the following settings outlined in Table 1.

Table 1. VNA settings.

Start Frequency (GHz)	Stop Frequency (GHz)	Intermediate Frequency (kHz)	Frequency Points
1	6.5	10	202

A positioning system was used to obtain a 100 × 100 2D raster scan spanning 0.94 × 0.94 m. Figure 1 shows an image of the positioning system, sand tank, VNA, and antenna used to acquire the measurements. The experimental system was originally developed for research on the characterisation of buried targets using high-lift-off polarimetric GPR, and it was found that the system could be readily adapted to the requirements of this study.

A single RAAC panel was used for all measurements; it was in generally good condition with minimal defects over the main body of the panel. However, the ends of the vertical sections of the reinforcement were exposed due to a break in the panel during the removal process. Assessing the corrosion condition of the exposed rebar revealed minimal rusting and good contact between the reinforcement and the concrete surround. There were also no visual signs of water ingress on the AAC itself. Three sets of results were obtained for the RAAC panel in different antenna elevations and angles. The elevations were 0.06, 0.18, and 0.2 m; the 0.06 m and 0.18 m elevations were positioned in a downward-looking configuration, whilst the 0.2 m elevation was angled at 20° from the vertical axis. A 20° angle was selected as a compromise to provide a sideways perspective, revealing the benefits of reduced reflected signals from the surface and also minimising ambiguity in the depth axis. The RAAC panel was positioned on the bed of sand and was raised with one and two sheets of radar absorbing material (RAM) for the 0.18/0.2 m and 0.06 m lift-off heights, respectively. The RAM not only helped to position the RAAC panel at the desired

height, but also reduced any parasitic late time reflections from the surface of the sand tank. The images shown in Figure 2 illustrate the setup for each configuration.

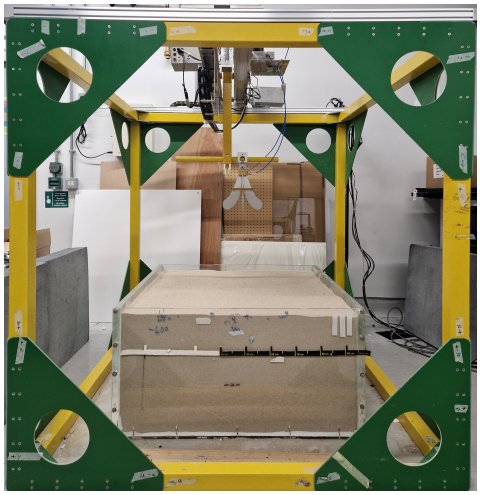

Figure 1. Experimental setup showing the positioning system, VNA, and dual-polarised antenna.

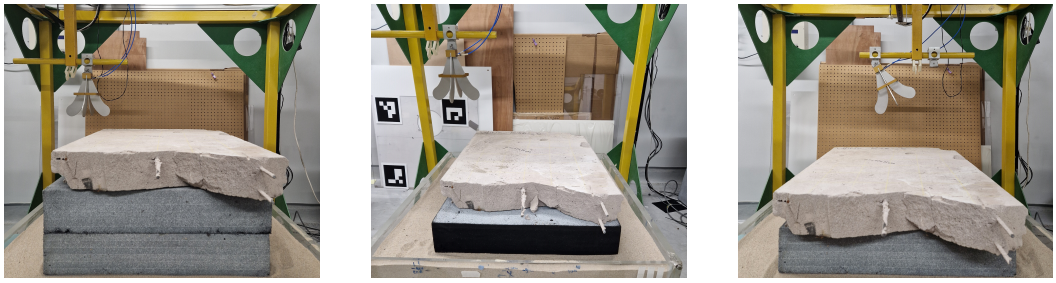

(**a**) (**b**) (**c**)

Figure 2. Images of the different RAAC configurations with 6 cm, 18 cm, and 20 cm lift-off distances. (**a**) Downward- looking configuration with 6 cm lift-off. (**b**) Downward-looking with 18 cm lift-off. (**c**) Sideways-looking with 20 cm lift-off and 20° angle.

2.2. Pre-Processing

Measurements from the VNA's S11 and S22 parameters presented a strong return reflection resulting from the impedance mismatch between the SMA connecting cable and the antenna. This confounded the small reflections obtained from the RAAC panel reinforcement. However, as this reflection remained relatively constant over multiple measurements, mitigating this effect by using a background measurement was possible. Therefore, a C-Scan measurement of the sand tank prior to placing the RAAC panel was obtained and subtracted from the subsequent RAAC measurements. This process removed the strong back reflection and additionally removed other signals from the clutter present in the environment.

Polarimetric antennas generally distort the calibrated VNA output; these distortions usually present as an imbalance in the magnitude and phase between co-polar channels and often poor cross-polar isolation. To ensure that the polarimetric data acquired matched the physical polarisation properties of the target, the polarimetric calibration of the antenna was performed using a methodology described in [42]. This aims to balance the magnitude and phase between co-polar channels and improve the cross-polar isolation. It provides more accurate polarimetric data and, as such, the reliable analysis and post-processing of the results can be performed. Without this procedure, the synthesised polarisation state would be distorted by the antenna and would not align with the intended polarisation state.

The processing of the obtained frequency-domain S-parameter data was as follows. Firstly, the time-domain signals of the C-Scan were obtained via a Hanning-windowed

inverse Fourier transform. These signals were then trimmed to align the start time of the measurements with the end of the antenna and the end time to shortly after the final RAAC pulse was received.

In order to accurately calculate the depth within the panel and the refraction angle between the air and the RAAC, the relative permittivity of the material is required. The relative permittivity of the RAAC that was used throughout this study was estimated using the panel thickness and the time delay in receiving the surface pulse and the underside pulse. A time delay of 0.48 ns and an RAAC thickness of 0.11 m resulted in a permittivity estimate of $\epsilon_r = 1.7$, a low value due to the high aeration and dry condition of the material.

2.3. 3D Polarimetric Synthetic Aperture Radar

The 3D polarimetric imaging algorithm has been developed and fully explained in [43]. A brief overview of the algorithm is given here; however, for full details, please refer to the referenced paper.

A forward model was developed to account for wave propagation within the system, incorporating a spherical wave path length and refraction at the air–medium boundary. Additional factors, including the antenna gain, transmit power, geometric spreading loss, and transmit wavelength, were considered to ensure alignment with the system's parameters. The lift-off of the antenna above the surface was sufficient such that the antenna was air-coupled; this required the calculation of the refraction in order to accurately capture the path length through two media.

The range to a potential target position can be separated into two lengths: the antenna to the surface and the surface to the target position. The range from the antenna to the surface is given by the Euclidean distance from these points (r_{1p}) [44],

$$r_{1p} = \sqrt{(x_{Ap} - X)^2 + (y_{Ap} - Y)^2 + (z_{Ap} - Z)^2} \tag{1}$$

where (x_{Ap}, y_{Ap}, z_{Ap}) are the antenna coordinates in 3D and (X, Y, Z) are the coordinates of the gridded surface area. The range in the second medium (r_{2p}) from the surface to a particular imaging depth (z_D) is calculated from the incident angle to the surface, using Snell's Law to calculate the transmitted angle. By combining the range calculations with Snell's Law, the Euclidean distance to a particular imaging depth can be calculated using Equation (2) [45]:

$$r_{2p} = \frac{z_D}{\sqrt{(1 - \frac{\epsilon_{r1}}{\epsilon_{r2}}) \cdot (1 - \left(\frac{z_{Ap}}{r_{1p}}\right)^2)}} \tag{2}$$

where ϵ_1 and ϵ_2 denote the relative permittivity of the the air and ground medium, respectively. Thus, the total path length is given by

$$r_p = r_{1p} + r_{2p}. \tag{3}$$

The equation that is solved for the inversion procedure is given by Equation (4) and follows the same methodology as [43]. This equation combines the range calculations into phase using k and r_p with the complex phasor. The expected receive voltage V_r for a particular transmit power, wavelength, range, antenna gain, and geometric spreading loss for an unknown reflectivity function σ is given by the radar range equation [46] and by rescaling the power to a voltage using the power equation [47,48].

$$V(x,y,z) = \iiint \sqrt{\sigma(x,y,z)} V_{r_{m1}}(x,y,z) V_{r_{m2}}(x,y,z) e^{-2i(k_{m1} r_{m1}(x,y,z) + k_{m2} r_{m2}(x,y,z))} \, dx \, dy \, dz \tag{4}$$

Here, $V_{r_{m1}}$ and $V_{r_{m2}}$ are the expected receive voltages for each medium derived from the radar equation [46], and the exponential term includes k_{m1} and k_{m2} for the wavenumbers

resulting in the phase lengths for medium 1 and medium 2, respectively. Equation (4) is now in the form $Ax = b$ and was solved using Tikhonov-regularised inversion. Solving for σ results in the images seen in the following sections.

2.4. Jones Vector Polarisation Synthesis

As mentioned in Section 2.3, for full details of the polarisation synthesis methodology, please refer to [43]. In this section, the synthesis of new polarisation states from the measured scattering matrix is performed using the Jones vector. The Jones vector is used to describe the polarisation state of a wave using the amplitudes A_x and A_y and phases δ_x and δ_y between the x and y components.

The Jones vector, representing the complex amplitude of the electric field, is given by [49–51]

$$\mathbf{E} = \begin{pmatrix} E_x \\ E_y \end{pmatrix} = \begin{pmatrix} A_x e^{i\delta_x} \\ A_y e^{i\delta_y} \end{pmatrix}. \tag{5}$$

Rewriting this in terms of the ellipticity χ and orientation φ angles, which describe the polarisation state of a wave, presents a more convenient representation for the parametrisation of the polarisation synthesis process [52]:

$$\mathbf{E} = \begin{pmatrix} \cos\chi\cos\varphi + i\sin\chi\sin\varphi \\ \cos\chi\sin\varphi - i\sin\chi\cos\varphi \end{pmatrix}. \tag{6}$$

To synthesise new polarisations from the scattering matrix, the Jones vector is used to represent the transmit E_t and receive E_r polarisations in the following equation [53]:

$$\mathbf{P_r}(\varphi_r, \chi_r, \varphi_t, \chi_t) = \left| \mathbf{E}_r(\varphi_r, \chi_r)^H \mathbf{S} \mathbf{E}_t(\varphi_t, \chi_t) \right|^2 \tag{7}$$

where P_r is the received power for the polarisation described by the transmit and receive Jones vectors applied to the scattering matrix S.

3. Results

3.1. Polarisation Components

In the following section, SAR images of the same RAAC panel are displayed for each polarisation component and for each measurement configuration; these results are normalised between 0 and 1 for easier interpretation of the relative signal levels between the polarisation components for each measurement configuration. The images shown are 2D slices of the 3D volume and were taken at a depth of 0.02 m, corresponding to the top portion of the reinforcement, while 3D isosurface representations are shown in Section 3.3. Two downward-looking measurements were obtained at 6 cm and 18 cm lift-off heights, as shown in Figure 3 and Figure 4, respectively, and a sideways-looking measurement was taken at a 20 cm height and a 20° angle from the vertical, as shown in Figure 5. In all these cases, a 2D reconstruction of the plane containing the top, i.e., the nearest layer, of the rebars is shown. This is at a depth of 2.0 cm inside the RAAC panel. The issues of reconstructing and presenting the entire 3D volume of the panel are addressed later in Section 3.3. These different configurations enable a comparison between the different potential acquisition modes. The internal structure of the RAAC panel is visible, showing the reinforcement in all three configurations. There are minimal observable differences between the two downward-looking configurations, highlighting the potential for higher-lift-off solutions for the detection of internal reinforcement within concrete structures. The 6 cm and 18 cm lift-off heights in Figure 3 and Figure 4 both capture the horizontal and vertical sections of the reinforcement in the co-polar HH and VV channels, respectively. The cross-polar

component is sensitive to the reinforcement intersection. Coupling the co- and cross-polar components reveals detailed information about the geometry of the reinforcement.

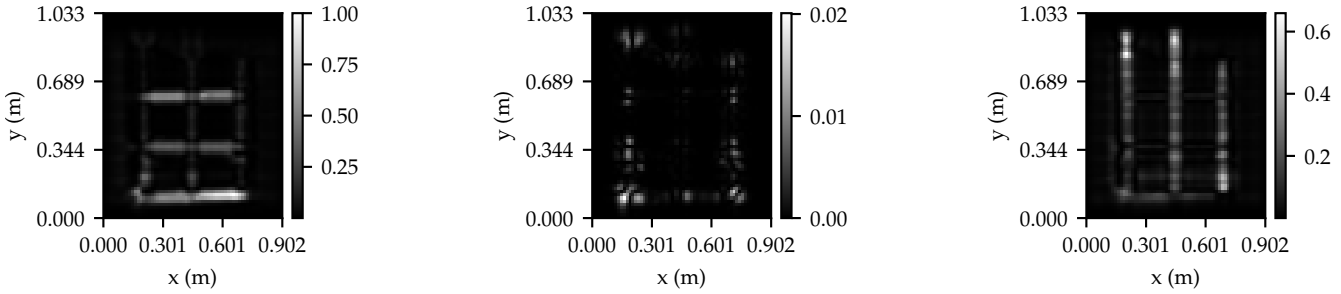

(**a**) (**b**) (**c**)

Figure 3. The 6 cm lift-off SAR images reconstructed at a depth of 2 cm, shown with (**a**) HH, (**b**) HV, and (**c**) VV polarisations.

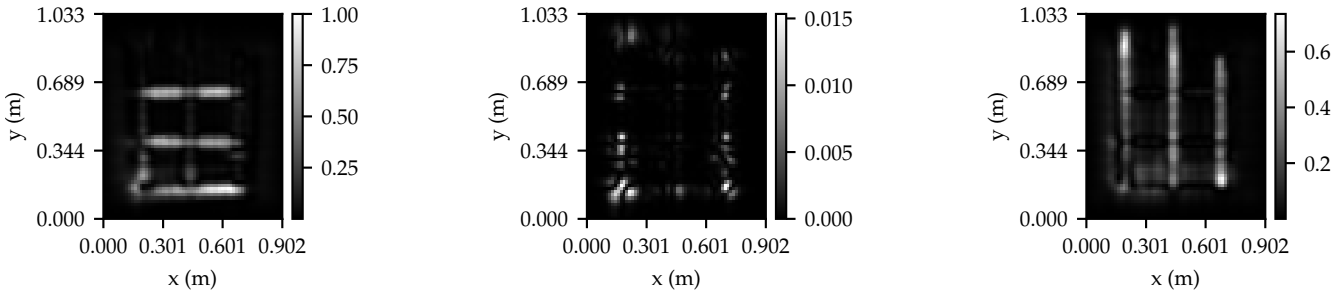

(**a**) (**b**) (**c**)

Figure 4. The 18 cm lift-off SAR images reconstructed at a depth of 2 cm, shown with (**a**) HH, (**b**) HV, and (**c**) VV polarisations.

The sideways-looking configuration, seen in Figure 5, illustrates different features and has the benefit of receiving a smaller signal from the air–concrete interface. The antenna alignment was such that the vertical co-polar channel was well aligned with the vertical reinforcement, whereas the horizontal co-polar component was affected by the tilt angle of the antenna. Both the HH and VV channels reveal the internal structure of the RAAC panel, displaying the horizontal and vertical sections; however, the reconstructed image has a different perspective due to the sideways view angle. The HH channel, shown in Figure 5a, detected both horizontal and vertical sections of the reinforcement; this acquisition mode has potential use for single polarisation systems that could be tilted, allowing for the detection of the full internal structure.

The sideways-looking cross-polar component in Figure 5b is more sensitive to the horizontal sections of the reinforcement, producing a consistent return along the length of the horizontal sections, as compared to the downward-looking measurements, which are more sensitive to the reinforcement intersections.

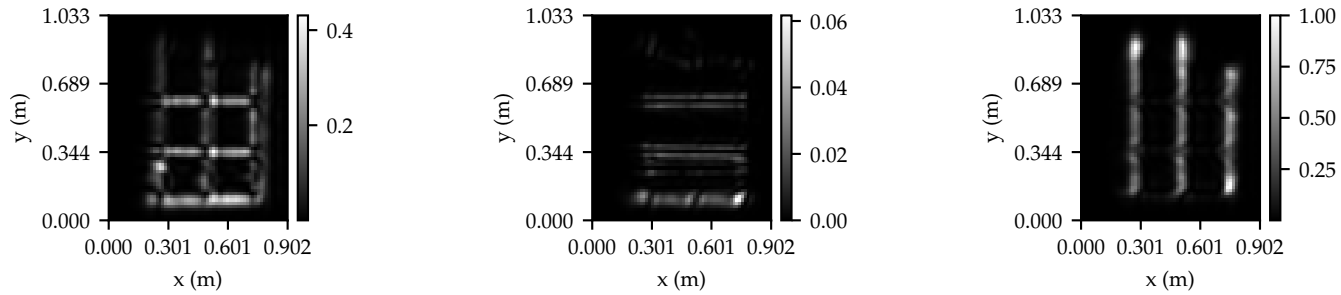

(**a**) (**b**) (**c**)

Figure 5. The 20 cm lift-off and 20° angle SAR images reconstructed at a depth of 2 cm, shown with (**a**) HH, (**b**) HV, and (**c**) VV polarisations.

3.2. Polarisation Synthesis

Polarisation synthesis provides an adaptable technique that can be used to enhance the detection and characterisation of targets by allowing the selection of the form of polarisation used. It can be seen that different polarisation states reveal different features of the target; the following section illustrates this by selecting three different types of polarisation, which include circular and elliptical polarisations. The chosen polarisation states for the downward-looking configurations are depicted in Table 2 and are defined by their ellipticity and orientation angles for both transmit and receive polarisations.

Table 2. Downward-looking polarisation states.

Polarisation	χ_{TX} (°)	χ_{RX} (°)	φ_{TX} (°)	φ_{RX} (°)
Right-hand circular (RHC)	45	45	-	-
Left-hand circular (LHC)	−45	−45	-	-
Left-hand elliptical (LHE)	−30	−30	50	50

Circular polarisations, as seen in Figures 6 and 7, are able to detect the reinforcement consistently and remove the orientation angle dependence of linear co-polar polarisations. This allows all reinforcements to be detected, regardless of the orientation, and displayed in one image. These images have a high signal-to-noise ratio as this polarisation is isolated from much of the co-polar background clutter. The chosen elliptical polarisation in Figures 6c and 7c illustrates the use of polarisation synthesis to selectively filter for different target features, such as highlighting the connecting reinforcement lengths separately. This can be seen for both downward-looking configurations; the balancing of the return signals from the horizontal and vertical sections of the rebar is achieved by tilting the orientation angle to 50°. This tilting of the orientation angle was required due to the difference in the return signal from the horizontal and vertical sections; the values selected were chosen through manual experimentation.

The resultant images produced from the sideways-looking configuration seen in Figure 8 require different polarisations to be selected to reveal distinct features, and these are displayed in Table 3. The angled perspective results in different cross-polar returns, and portions of the horizontal and vertical reinforcement are measured by the HH polarisation component, as shown in Figure 5a. This mode still provides benefits, as seen with the single polarisation HH channel, which can effectively capture most of the reinforcement with a single polarisation channel.

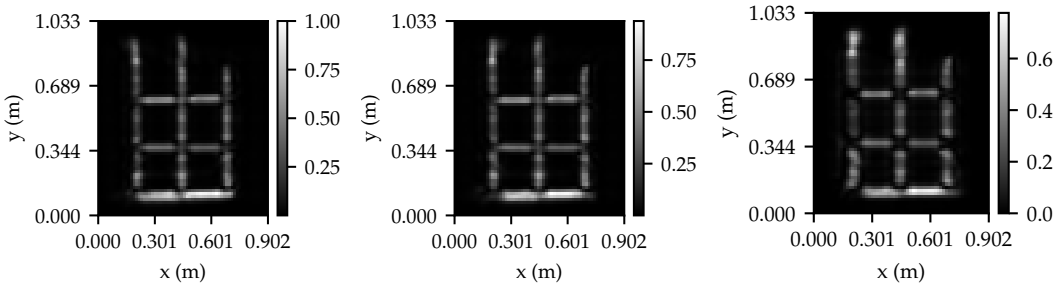

(**a**) (**b**) (**c**)

Figure 6. The 6 cm lift-off polarisation synthesised SAR images reconstructed at a depth of 2 cm, shown with (**a**) RHC, (**b**) LHC, and (**c**) LHE polarisations.

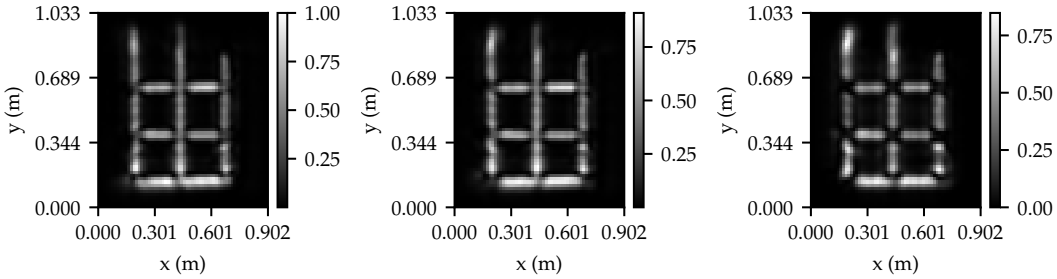

(**a**) (**b**) (**c**)

Figure 7. The 18 cm lift-off polarisation synthesised SAR images reconstructed at a depth of 2 cm, shown with (**a**) RHC, (**b**) LHC, and (**c**) LHE polarisations.

Table 3. Sideways-looking polarisation states

Polarisation	χ_{TX} (°)	χ_{RX} (°)	φ_{TX} (°)	φ_{RX} (°)
RHC	45	45	-	-
LHC	−45	−45	-	-
45° Cross-polar	0	0	−45	45

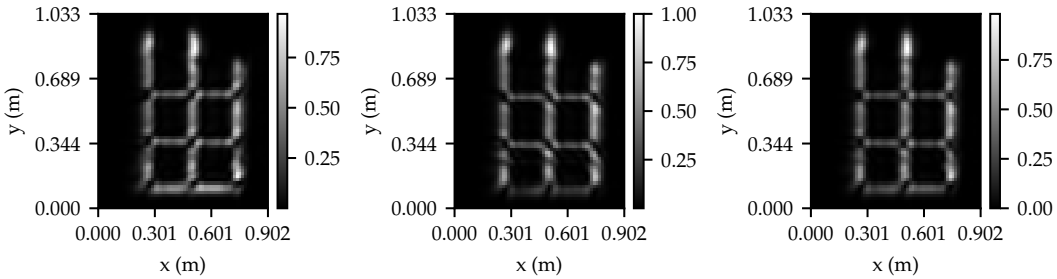

(**a**) (**b**) (**c**)

Figure 8. The 20 cm lift-off 20° angle polarisation synthesised SAR images reconstructed at a depth of 2 cm, shown with (**a**) RHC, (**b**) LHC, and (**c**) 45° cross-polar polarisations.

The circular polarisation images for the sideways-looking configuration seen in Figure 8a,b are still able to detect the reinforcement consistently, similarly to the downward-looking configuration. The intersections of the reinforcement have angled breaks within the image, which reverse for right-hand and left-hand circular polarisations; these can be balanced by selecting a cross-polar polarisation state that is at a 45° orientation angle, aligning this result more closely with the downward-looking configurations. This is illustrated in Figure 8c.

Figure 9 shows a cross-section of the horizontal and vertical reinforcement. The signal-to-noise ratio and resolution can be compared between the different measurement configurations and polarisations. For example, HH compared with RHC polarisation in Figure 9a,c shows that RHC provides a slight improvement in target localisation. Additionally, the comparison between VV and RHC illustrates a more significant improvement in signal to noise by the order of approximately 10 dB. This improvement is attributed to the higher surface reflection in the co-polar channels, which circular polarisation more effectively rejects. This difference is less noticeable for the sideways-looking configuration shown in Figure 9e,f, where the co-polar surface reflection is less of a factor aligning HH/VV and RHC more closely.

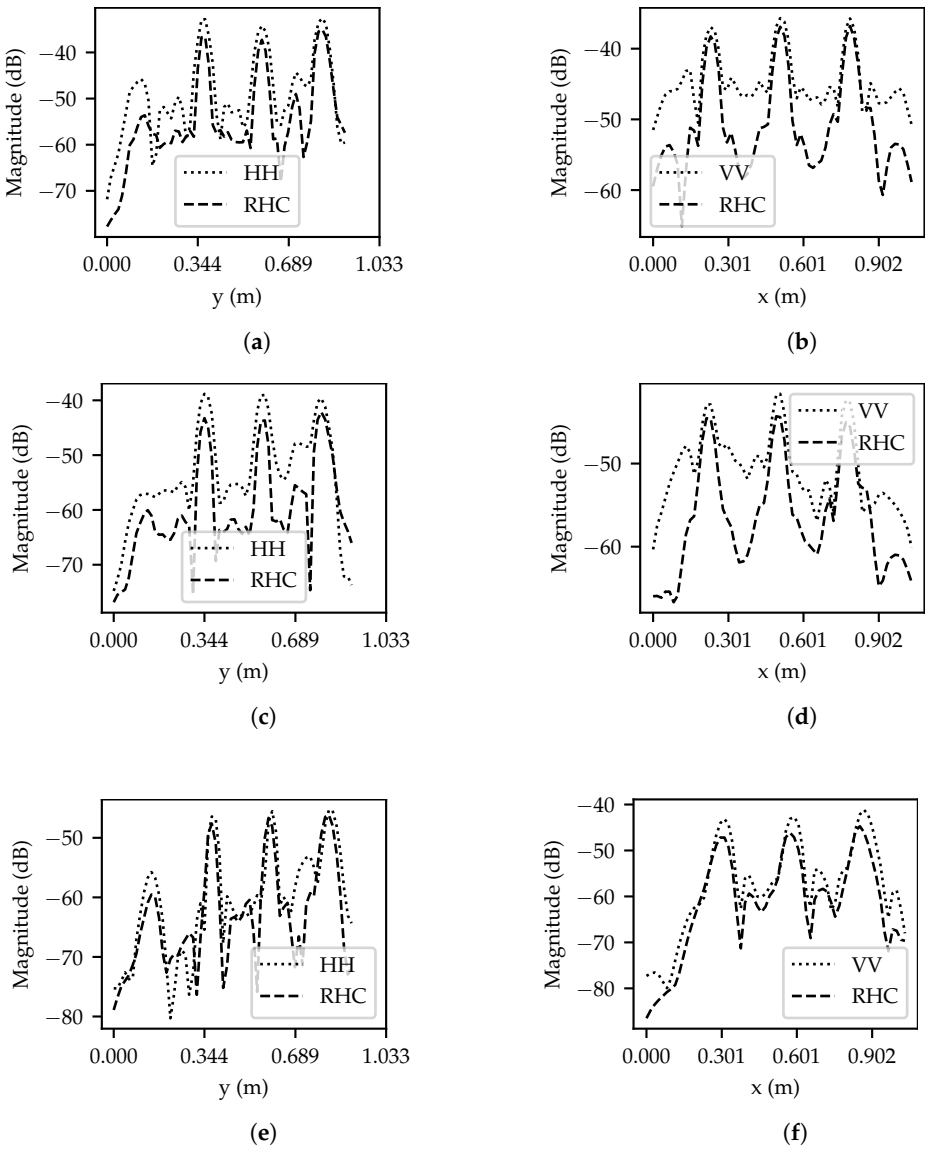

Figure 9. Cross-section of horizontal and vertical reinforcement with (**a**)—HH/RHC at 6 cm lift-off, (**b**)—VV/RHC at 6 cm lift-off, (**c**)—HH/RHC at 18 cm lift-off, (**d**)—VV/RHC at 18 cm lift-off, (**e**)—HH/RHC at 20 cm lift-off and 20° angle, and (**f**)—VV/RHC at 20 cm lift-off and 20° angle.

3.3. 3D Image Representations

Thus far, 2D slices of the 3D volume have been shown; however, the SAR algorithm produces volumetric data, and, as such, it may be useful to represent the internal RAAC structure in 3D. The 3D visualisation has been achieved using isosurfaces, where the higher-amplitude portions of the return signal are represented as a solid surface. The following images show the full depth of the RAAC panel with each polarisation component. An additional feature is seen in the horizontal component when observing the full depth profile of the RAAC panel in both the 6 cm and 18 cm downward-looking configurations in Figure 10a and Figure 10b, respectively. This feature is associated with an air cavity that runs horizontally through the entire panel, illustrating the sensitivity of GPR in detecting structural defects. This can be seen more clearly in Figure 11. In Figure 10c,f,i, we illustrate a vertical section below the reinforcement, which is due to an air cavity between the RAAC concrete and RAM sheet. This is also visualised in Figure 11.

Comparatively, the vertical component of the sideways-looking result in Figure 10i illustrates a similar profile to the downward-looking configurations, as this component is

aligned to the vertical reinforcement; however, the horizontal component in Figure 10g is more affected by the tilt angle, which displays both horizontal and vertical components. The cross-polar component of the sideways-looking image in Figure 10h compared to the downward-looking images in Figure 10b,e can be clearly seen, with the intersections of the reinforcement visible in the downward-looking case and the horizontal reinforcement with the sideways-looking case.

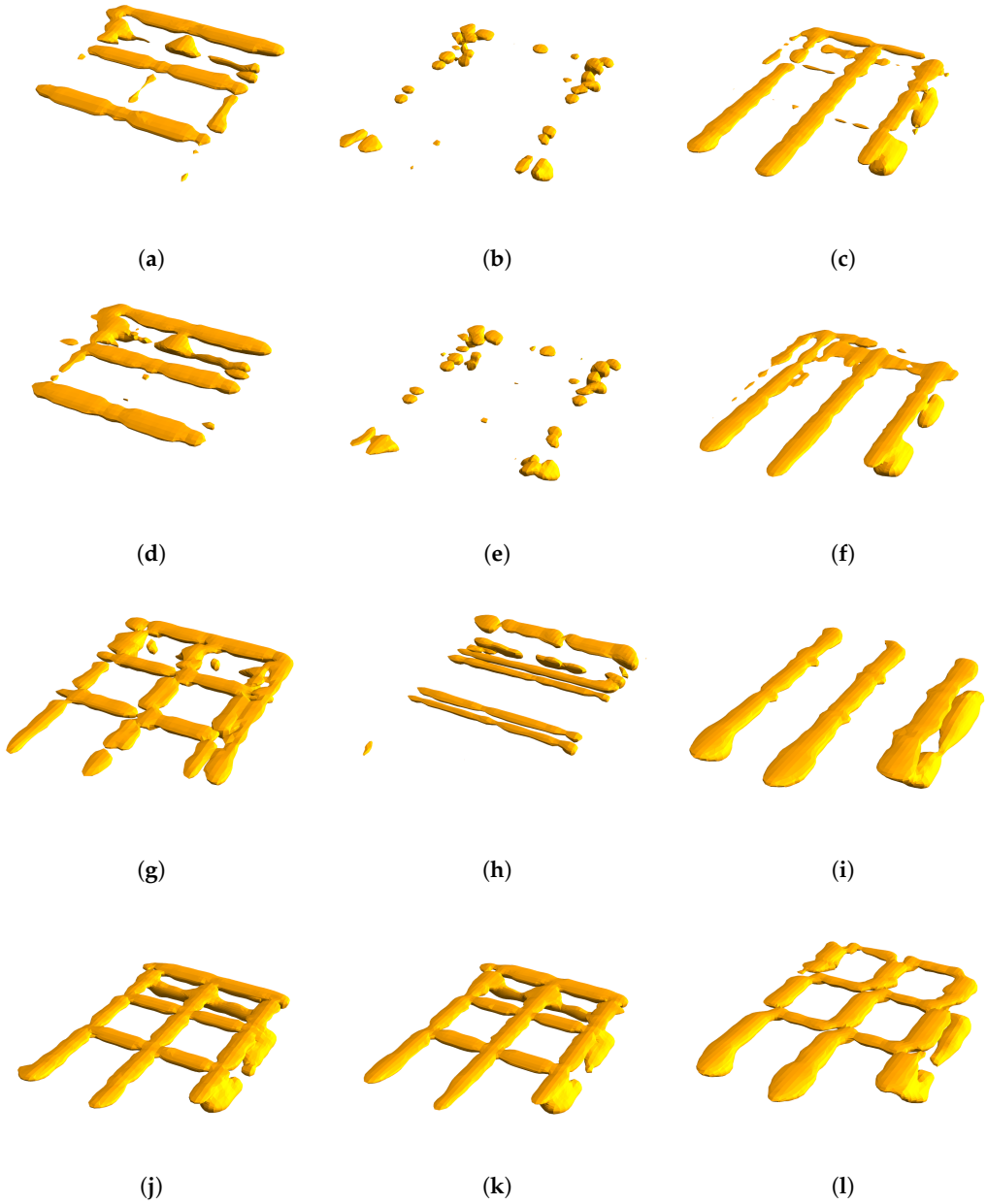

Figure 10. Isosurface representations of the internal reinforcement with measurement configurations and polarisations as follows: (**a**)—HH at 6 cm lift-off, (**b**)—HV at 6 cm lift-off, (**c**)—VV at 6 cm lift-off, (**d**)—HH at 18 cm lift-off, (**e**)—HV at 18 cm lift-off, (**f**)—VV at 18 cm lift-off, (**g**)—HH at 20 cm lift-off and 20 ° angle, (**h**)—HV at 20 cm lift-off and 20 ° angle, (**i**)—VV at 20 cm lift-off and 20 ° angle, (**j**)—RHC at 6 cm lift-off, (**k**)—RHC at 18 cm lift-off, and (**l**)—RHC at 20 cm lift-off and 20 ° angle.

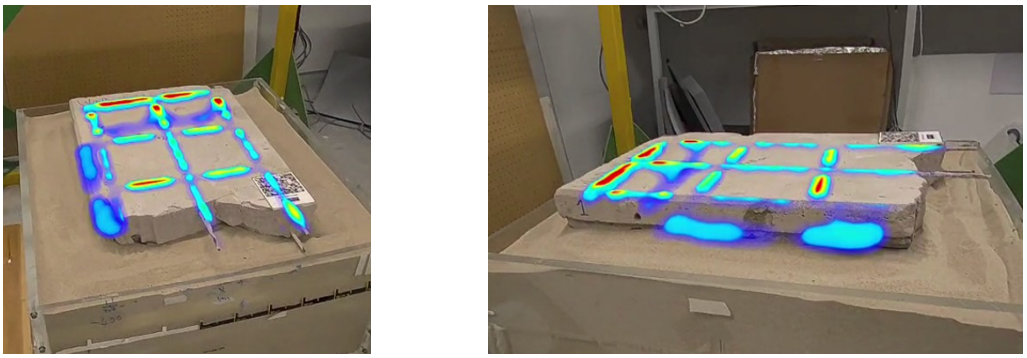

(a) (b)

Figure 11. AR volume rendering of 18 cm lift-off result with RHC polarisation with two visual perspectives (**a**,**b**).

In Figure 10j–l, a right-hand circular polarisation was used to create a 3D isosurface representation of the internal RAAC structure. Both downward-looking configurations in Figure 10j,k reveal very similar features, as seen in the previous section. However, the sideways-looking angle seen in Figure 10l has a slight perspective shift due to the angled view, although it still captures many of the same features. The upper portion of the reinforcement is well resolved and the air cavity has improved visibility when using circular polarisation, which can be seen between the first two upper horizontal sections. The vertical section of the lower air cavity is also visible. Contrasting the circular polarisation isosurfaces with the single polarisation results shows the improved resolution of the reinforcement structure and lower clutter within the imaged area.

3.4. Augmented Reality

Augmented reality (AR) is emerging as a valuable tool to enhance the interpretation of complex NDT data. AR visualisation of subsurface features is effective with GPR when overlaying data sets directly onto physical structures, as demonstrated by Pereira et al. in [54]. In addition to visualisation, the optical tracking elements of AR devices have been used to index the positions of GPR units in areas where GPS data are unreliable [55]. Light detection and ranging (LiDAR) sensors can complement GPR data by returning detailed surface information to assist in interpreting subsurface features [56]. These sensors also support the spatial mapping capabilities of AR devices, which can be fused to align GPR scans with surface topography [57]. Handheld devices such as Screening Eagle's GPR Live exemplify the growing adoption of portable AR-integrated solutions in the field [58]. Inspectors can achieve an "X-ray vision" effect, where buried utilities, reinforcing bars, cracks, and voids are projected onto the surface of a structure in real time, enhancing situational awareness and reducing the reliance on invasive techniques. However, achieving this effect on-site and in real time requires further work to improve the depth perception of superimposed objects, automatic pose estimation, and rendering optimisation [59,60]. In this study, a custom AR application was created in Unity using the Vuforia engine, integrating optical tracking algorithms to superimpose GPR data onto physical samples. The processed 3D data, parsed with an open-source volume rendering tool [61], were displayed on Meta Quest 3 and HoloLens 2 head-mounted devices (HMDs) for hands-free visualisation. Natural feature image tracking was employed to ensure the accurate alignment of the digital data with the physical sample by using a fiducial marker placed at a fixed position relative to the structure. This approach allows the spatial pose of the image to be computed relative to the HMD's cameras, enabling the precise overlay of the isosurfaces onto the structure. Figure 11 shows an image from the HMD; the data are highly contrasted against the sample, aligning closely with the observable rebar.

The practical applications of this technology extend beyond basic visualisation. In field inspections, AR can reduce uncertainty about the precise locations of structural elements, such as reinforcing bars, which would traditionally require invasive methods like drilling or probing to verify. Furthermore, AR-based systems have the potential to support long-term, large-scale structural monitoring. By automatically indexing data against position during routine inspections and integrating additional metrics, such as LiDAR surface scans, AR can be used to create temporal digital twins. These digital models offer a comprehensive and evolving depiction of the structural integrity, making data interpretation, storage, and sharing simpler.

4. Conclusions

Using polarimetry to image the internal structures of RAAC panels has been demonstrated to be a flexible and powerful technique. Measuring the full polarimetric data and using the principle of polarisation synthesis can improve the reconstruction of the internal reinforcement; this methodology can be applied in real time and also in post-processing, allowing a more detailed investigation into the RAAC properties. The comparison between two downward-looking lift-off heights demonstrates the potential for the development of systems with higher lift-off, offering greater flexibility in the choice of the acquisition mode. Additionally, this approach provides significant health and safety benefits by ensuring that asbestos coatings remain undisturbed, which is highly desirable in healthcase estates, where RAAC is commonplace. This allows the measurement of panels using handheld systems by removing the orientation angle dependence with circular polarisation, and the high lift-off scenario has potential for use with drones for less accessible areas. Sideways-looking results have shown benefits in revealing the internal structure with a single polarisation and a reduced signal from the air–concrete interface, improving the signal-to-noise ratio and thus illustrating another viable acquisition mode. Additionally, integrating polarisation synthesis with AR has been shown to have potential as it could be used for real-time inspection using handheld devices; overlaying supplementary sensor data could give a user more detailed metrics for the determination of the positions of reinforcement and potential degradation. GPR has been shown to detect not only the metal reinforcement but also air cavities, which can aid in the assessment, and has the potential to detect other defects, such as water ingress.

5. Future Work

In this study, reliably detecting the lower layer of reinforcement was challenging. Therefore, investigating a non-contact modality that allows the imaging of the lower layer of reinforcement would be highly beneficial. This may involve a closer sideways-looking measurement with a more directional antenna.

Additionally, defects such as water ingress would be visible to GPR due to the high permittivity of water, creating a strong contrast with the surrounding material. As such, artificially inducing water ingress and monitoring the condition of the RAAC panels using GPR would be a worthwhile investigation.

Further work aimed at the development of a non-contact handheld detector would have significant industrial applications and would provide substantial health and safety benefits.

Author Contributions: Conceptualization, S.J.I.F., D.C., A.J.P., F.J.W.P., N.D. and J.B.E.; Data curation, S.J.I.F. and D.C.; Formal analysis, S.J.I.F., A.J.P. and F.J.W.P.; Funding acquisition, A.J.P., F.J.W.P. and N.D.; Investigation, S.J.I.F. and D.C.; Methodology, S.J.I.F., D.C., A.J.P. and F.J.W.P.; Project administration, A.J.P., F.J.W.P. and N.D.; Resources, A.J.P., F.J.W.P. and J.B.E.; Software, S.J.I.F. and D.C.; Supervision, A.J.P., F.J.W.P. and N.D.; Validation, S.J.I.F., A.J.P. and F.J.W.P.; Visualization, S.J.I.F.

and D.C.; Writing—original draft, S.J.I.F. and D.C.; Writing—review and editing, S.J.I.F., D.C, A.J.P., F.J.W.P., N.D. and J.B.E. All authors have read and agreed to the published version of the manuscript.

Funding: This research is funded by the Engineering and Physical Sciences Research Council (EPSRC) and the Defence Science and Technology Laboratory (Dstl), under iCASE voucher 19000062.

Data Availability Statement: The data supporting this study are available from the corresponding author upon reasonable request. Access to the data may be granted after obtaining the necessary permissions.

Conflicts of Interest: The authors declare no conflicts of interest.

References

1. Saad, A.M.; Gorse, C.; Goodier, C.I.; Blay, K.; Cavalaro, S. Autoclaved Aerated Concrete in Reinforced Building Applications: A Systematic Review of AAC/RAAC in the Last 40+ Years. *Results Eng.* **2024**, *24*, 103431. [CrossRef]
2. Jeong, H.; Takahashi, H.; Teramura, S. Low temperature fracture behaviour and AE characteristics of autoclaved aerated concrete(AAC). *Cem. Concr. Res.* **1987**, *17*, 743–754. [CrossRef]
3. Fouad, F.H.; Schoch, T. AAC in the USA—A second look. *ce/papers* **2018**, *2*, E1–E6. [CrossRef]
4. Liddell, M.; Read, R.; Palmer, M.; Robertson, D.; Goodier, C. *Reinforced Autoclaved Aerated Concrete (RAAC) Panels: Investigation and Assessment*; Technical Report; The Institution of Structural Engineers RAAC Inspection and Assessment: London, UK, 2022.
5. Di Sarno, L.; Albuhairi, D. Reinforced Autoclaved Aerated Concrete: Structural Assessment and Retrofitting. *Buildings* **2024**, *14*, 2570. [CrossRef]
6. Cabrera, J. Deterioration of concrete due to reinforcement steel corrosion. *Cem. Concr. Compos.* **1996**, *18*, 47–59. [CrossRef]
7. Broomfield, J.P. *Corrosion of Steel in Concrete: Understanding, Investigation and Repair*; CRC Press: Boca Raton, FL, USA, 2023.
8. Fang, C.; Lundgren, K.; Chen, L.; Zhu, C. Corrosion influence on bond in reinforced concrete. *Cem. Concr. Res.* **2004**, *34*, 2159–2167. [CrossRef]
9. Cheng, W.; Fan, Z.; Tan, K.H. Characterisation of corrosion-induced crack in concrete using ultrasonic diffuse coda wave. *Ultrasonics* **2023**, *128*, 106883. [CrossRef]
10. Larose, E.; Planes, T.; Rossetto, V.; Margerin, L. Locating a small change in a multiple scattering environment. *Appl. Phys. Lett.* **2010**, *96*, 204101. [CrossRef]
11. Song, W.J.; Popovics, J.S.; Aldrin, J.C.; Shah, S.P. Measurement of surface wave transmission coefficient across surface-breaking cracks and notches in concrete. *J. Acoust. Soc. Am.* **2003**, *113*, 717–725. [CrossRef] [PubMed]
12. Cheng, W.; Sun, H.H.; Wan, L.S.; Fan, Z.; Tan, K.H. Corrosion damage detection in reinforced concrete using Rayleigh wave-based method. *Cem. Concr. Compos.* **2023**, *143*, 105253. [CrossRef]
13. *ASTM C876-91*; Standard Test Method for Half-Cell Potentials of Uncoated Reinforcing Steel in Concrete. ASTM: West Conshohocken, PA, USA, 1999; Volume 3.
14. Elsener, B.; Andrade, C.; Gulikers, J.; Polder, R.; Raupach, M. Half-cell potential measurements—Potential mapping on reinforced concrete structures. *Mater. Struct.* **2003**, *36*, 461–471. [CrossRef]
15. Zhang, J.; Liu, C.; Sun, M.; Li, Z. An innovative corrosion evaluation technique for reinforced concrete structures using magnetic sensors. *Constr. Build. Mater.* **2017**, *135*, 68–75. [CrossRef]
16. Gu, P.; Elliott, S.; Hristova, R.; Beaudoin, J.; Brousseau, R.; Baldock, B. A study of corrosion inhibitor performance in chloride contaminated concrete by electrochemical impedance spectroscopy. *ACI Mater. J.* **1997**, *94*, 385–395.
17. Ford, S.; Shane, J.; Mason, T. Assignment of features in impedance spectra of the cement-paste/steel system. *Cem. Concr. Res.* **1998**, *28*, 1737–1751. [CrossRef]
18. Poupard, O.; Aıt-Mokhtar, A.; Dumargue, P. Corrosion by chlorides in reinforced concrete: Determination of chloride concentration threshold by impedance spectroscopy. *Cem. Concr. Res.* **2004**, *34*, 991–1000. [CrossRef]
19. Andrade, C.; González, J. Quantitative measurements of corrosion rate of reinforcing steels embedded in concrete using polarization resistance measurements. *Mater. Corros.* **1978**, *29*, 515–519. [CrossRef]
20. Clear, K.C. *Measuring Rate of Corrosion of Steel in Field Concrete Structures*; Transportation Research Record; The National Academies of Sciences, Engineering, and Medicine: Washington, DC, USA, 1989.
21. Andrade, C.; Alonso, M.C.; Gonzalez, J.A. An initial effort to use the corrosion rate measurements for estimating rebar durability. In *Corrosion Rates of Steel in Concrete*; ASTM International: West Conshohocken, PA, USA, 1990.
22. Newton, C.; Sykes, J. A galvanostatic pulse technique for investigation of steel corrosion in concrete. *Corros. Sci.* **1988**, *28*, 1051–1074. [CrossRef]
23. Sathiyanarayanan, S.; Natarajan, P.; Saravanan, K.; Srinivasan, S.; Venkatachari, G. Corrosion monitoring of steel in concrete by galvanostatic pulse technique. *Cem. Concr. Compos.* **2006**, *28*, 630–637. [CrossRef]

24. Vedalakshmi, R.; Balamurugan, L.; Saraswathy, V.; Kim, S.H.; Ann, K. Reliability of Galvanostatic Pulse Technique in assessing the corrosion rate of rebar in concrete structures: Laboratory vs field studies. *KSCE J. Civ. Eng.* **2010**, *14*, 867–877. [CrossRef]
25. Elyasigorji, A.; Rezaee, M.; Ghorbanpoor, A. Magnetic corrosion detection in concrete structures. In Proceedings of the International Conference on Sustainable Infrastructure, Los Angeles, CA, USA, 6–9 November 2019; American Society of Civil Engineers Reston: Reston, VA, USA, 2019; pp. 175–184.
26. Shams, S.; Ghorbanpoor, A.; Lin, S.; Azari, H. Nondestructive Testing of Steel Corrosion in Prestressed Concrete Structures using the Magnetic Flux Leakage System. *Transp. Res. Rec.* **2018**, *2672*, 132–144. [CrossRef]
27. Yang, D.; Qiu, J.; Di, H.; Zhao, S.; Zhou, J.; Yang, F. Quantitative Evaluation of Corrosion Degrees of Steel Bars Based on Self-Magnetic Flux Leakage. *Metals* **2019**, *9*, 952. [CrossRef]
28. de Alcantara, N.P., Jr.; Da Silva, F.M.; Guimarães, M.T.; Pereira, M.D. Corrosion assessment of steel bars used in reinforced concrete structures by means of eddy current testing. *Sensors* **2015**, *16*, 15. [CrossRef] [PubMed]
29. Eddy, I.; Underhill, P.R.; Morelli, J.; Krause, T.W. Pulsed Eddy Current Response to General Corrosion in Concrete Rebar. *J. Nondestruct. Eval. Diagn. Progn. Eng. Syst.* **2020**, *3*, 044501. [CrossRef]
30. Rahita, A.C.; Zaki, A. Corrosion Analysis on Reinforcing Steel in Concrete Using the Eddy Current Method. In Proceedings of the 2023 3rd International Conference on Electronic and Electrical Engineering and Intelligent System (ICE3IS), Yogyakarta, Indonesia, 9–10 August 2023; pp. 476–480. [CrossRef]
31. Dérobert, X.; Aubagnac, C.; Abraham, O. Comparison of NDT techniques on a post-tensioned beam before its autopsy. *NDT E Int.* **2002**, *35*, 541–548. [CrossRef]
32. Roqueta, G.; Jofre, L.; Feng, M.Q. Analysis of the Electromagnetic Signature of Reinforced Concrete Structures for Nondestructive Evaluation of Corrosion Damage. *IEEE Trans. Instrum. Meas.* **2012**, *61*, 1090–1098. [CrossRef]
33. Tešić, K.; Baričević, A.; Serdar, M. Non-Destructive Corrosion Inspection of Reinforced Concrete Using Ground-Penetrating Radar: A Review. *Materials* **2021**, *14*, 975. [CrossRef]
34. Zaki, A.; Megat Johari, M.A.; Wan Hussin, W.M.A.; Jusman, Y. Experimental Assessment of Rebar Corrosion in Concrete Slab Using Ground Penetrating Radar (GPR). *Int. J. Corros.* **2018**, *2018*, 5389829. [CrossRef]
35. Chang, C.W.; Lin, C.H.; Lien, H.S. Measurement radius of reinforcing steel bar in concrete using digital image GPR. *Constr. Build. Mater.* **2009**, *23*, 1057–1063. [CrossRef]
36. Hugenschmidt, J.; Kalogeropoulos, A.; Soldovieri, F.; Prisco, G. Processing strategies for high-resolution GPR concrete inspections. *NDT E Int.* **2010**, *43*, 334–342. [CrossRef]
37. Elliott, J.B.; Chaney, D.; Murtaza, H. Angled ground penetrating radar to detect and position reinforcement and bearing lengths within reinforced autoclaved aerated concrete planks. *Constr. Build. Mater.* **2024**, *449*, 138528. [CrossRef]
38. Liu, H.; Zhong, J.; Ding, F.; Meng, X.; Liu, C.; Cui, J. Detection of early-stage rebar corrosion using a polarimetric ground penetrating radar system. *Constr. Build. Mater.* **2022**, *317*, 125768. [CrossRef]
39. Benedetto, A.; Manacorda, G.; Simi, A.; Tosti, F. Novel perspectives in bridges inspection using GPR. *Nondestruct. Test. Eval.* **2012**, *27*, 239–251. [CrossRef]
40. Pasculli, D.; Natali, A.; Salvatore, W.; Morelli, F.; Morandi, D. Investigation of reinforced concrete bridges by using a dual-polarized high-frequency GPR. In Proceedings of the 2018 17th International Conference on Ground Penetrating Radar (GPR), Rapperswil, Switzerland, 18–21 June 2018; pp. 1–5. [CrossRef]
41. Noonan, C. Environmental asbestos exposure and risk of mesothelioma. *Ann. Transl. Med.* **2017**, *5*, 234. [CrossRef] [PubMed]
42. Forster, S.J.I.; Peyton, A.J.; Podd, F.J.W. Calibration of dual-polarised antennas for air-coupled ground penetrating radar applications. *Remote Sens.* **2024**, *16*, 4114. [CrossRef]
43. Forster, S.J.I.; Peyton, A.J.; Podd, F.J.W.; Davidson, N. Polarisation Synthesis Applied to 3D Polarimetric Imaging for Enhanced Buried Object Detection and Identification. *Remote Sens.* **2024**, *16*, 4279. [CrossRef]
44. Strang, G. *Introduction to Linear Algebra*; Wellesley-Cambridge Press: Wellesley, MA, USA, 2009.
45. Hecht, E. *Optics*, 4th ed.; Pearson Education Limited: Harlow, UK, 2014; p. 680.
46. Skolnik, M.I. *Introduction to Radar Systems*; McGraw-Hill: New York, NY, USA, 1962.
47. Ohm, G.S. *Die Galvanische Kette, Mathematisch Bearbeitet*; Riemann: Berlin, Germany, 1827.
48. Joule, J.P. On the heat evolved by metallic conductors of electricity, and in the cells of a battery during electrolysis. *Philos. Mag.* **1841**, *19*, 260–277. [CrossRef]
49. Jones, R.C. A new calculus for the treatment of optical systems I. Description and discussion of the calculus. *J. Opt. Soc. Am.* **1941**, *31*, 488–493. [CrossRef]
50. Hurwitz, H.; Jones, R.C. A new calculus for the treatment of optical systems II. Proof of three general equivalence theorems. *J. Opt. Soc. Am.* **1941**, *31*, 493–499. [CrossRef]
51. Jones, R.C. New calculus for the treatment of optical systems. III. The Sohncke theory of optical activity. *J. Opt. Soc. Am.* **1941**, *31*, 500. [CrossRef]

52. Huynen, J.R. Phenomenological Theory of Radar Targets. Ph.D. Thesis, Technical University of Delft, Delft, The Netherlands, 1970.
53. Yang, R.; Dai, B.; Tan, L.; Liu, X.; Yang, Z.; Li, H. *Polarimetric Microwave Imaging*; Springer: Singapore, 2021; pp. 52–58. [CrossRef]
54. Pereira, M.; Burns, D.; Orfeo, D.; Zhang, Y.; Jiao, L.; Huston, D.; Xia, T. 3-D Multistatic Ground Penetrating Radar Imaging for Augmented Reality Visualization. *IEEE Trans. Geosci. Remote Sens.* **2020**, *58*, 5666–5675. [CrossRef]
55. Childs, J.; Orfeo, D.; Burns, D.; Huston, D.; Xia, T. Enhancing ground penetrating radar with augmented reality systems for underground utility management. In Proceedings of the Virtual, Augmented, and Mixed Reality (XR) Technology for Multi-Domain Operations, Online, 27 April–8 May 2020; Dennison, M.S., Jr., Ed.; International Society for Optics and Photonics, SPIE: Bellingham, WA, USA, 2020; Volume 11426, p. 1142608. [CrossRef]
56. Berezowski, V.; Moffat, I.; Shendryk, Y.; MacGregor, D.; Ellis, J.; Mallett, X. A multidisciplinary approach to locating clandestine gravesites in cold cases: Combining geographic profiling, LiDAR, and near surface geophysics. *Forensic Sci. Int. Synerg.* **2022**, *5*, 100281. [CrossRef] [PubMed]
57. Voordijk, H.; olde Scholtenhuis, L. Technological mediation and 3D visualizations in construction engineering practice. *AI Soc.* **2024**, *39*, 207–220. [CrossRef]
58. Screening Eagle Technologies. Leveraging Augmented Reality to Save Money—And Lives. 2024. Available online: https://www.screeningeagle.com/en/about-us/news/leveraging-augmented-reality-to-save-money%E2%80%93and-lives (accessed on 6 January 2024).
59. Clarke, T.J.; Gwilt, I.; Zucco, J.; Mayer, W.; Smith, R.T. Superpowers in the Metaverse: Augmented Reality Enabled X-Ray Vision in Immersive Environments. In *Augmented and Virtual Reality in the Metaverse*; Geroimenko, V., Ed.; Springer Nature: Cham, Switzerland, 2024; pp. 283–309. [CrossRef]
60. Prinz, L.M.; Mathew, T. Support Lines and Grids for Depth Ordering in Indoor Augmented Reality using Optical See-Through Head-Mounted Displays. In Proceedings of the 2024 ACM Symposium on Spatial User Interaction, New York, NY, USA, 7–8 October 2024; SUI '24. [CrossRef]
61. Lavik, M. UnityVolumeRendering. 2024. Available online: https://github.com/mlavik1/UnityVolumeRendering (accessed on 20 November 2024).